Chapter 4

Observation of the multiple magnetic phases in double perovskite $Pr_{1.8}La_{0.2}CoFeO_6$

4.1 Introduction

The increased demand for next-generation spintronic devices has triggered scientists and researchers to search for multifunctional materials [92,93]. In search of materials having strongly correlated magnetic and electrical properties, the researchers are attracted particularly to the family of double perovskite (DP’s) $R_2B'B''O_6$ due to its wide range of exotic properties, including giant magneto-caloric effects, magneto-resistance, anti-site disorder-driven multiclass phase, Griffiths phase (GP), exchange bias (EB), meta-magnetic transition, the magneto-dielectric effect, etc. [94–101]., those can be used to design unique devices with useful applications. The double perovskite structure ($R_2B'B''O_6$) consists of two conventional perovskite unit cells, with B and B' cations forming a rock-salt-like pattern (checkerboard design). The majority of Fe/Co/Ni (B) - Mn (B') based ordered DP's exhibit high-temperature magnetic transition due to 180^0 FM super-exchange interactions between B^{2+} and B'^{4+} cations (partially filled d-orbital), which is well explained by Goodenough-Kanamori law [2,3]. Anti-site disorder in double perovskite, or a mutual exchange of B/B' positions, is well recognized to have a significant influence on their structural characteristics, mainly their magnetic features, requiring thorough research in both theory and experiment [102,103]. Furthermore, the anti-site disorder may produce additional AFM clustered regions via superexchange interactions in the form of B^{2+}-O^{2-}-B^{2+} and Mn^{4+}-O^{2-}-Mn^{4+}, which in turn leads to competition between AFM and FM interactions. It is well-known that competing AFM and FM interactions are the key factors in predicting the development of short-range ordering-associated secondary magnetic phases. These phases include Griffiths phase, low-temperature spin-glass, and exchange bias amongst others. The research on the Fe-based DPs, or R_2BFeO_6 oxides, is comparatively less in comparison to the widely studied R_2BMnO_6 (R = Dy, Y, Pr, La, Ho, etc. and B = Mn, Co, etc.) compounds, providing a variety of fascinating physical properties. It is claimed that the B^{3+} and B'^{3+} ions generally increase anti-site disorder through random site distribution at the octahedral sites, leading to rhombohedra or orthorhombic (Pnma) structures [104,105]. Therefore, the B^{3+} and Fe^{3+} ions in R_2BFeO_6 systems provide a significant anti-site disorder, which has tremendous potential to contribute to a variety of outstanding characteristics as stated above. Compounds in which the A site is occupied by a magnetically active rare earth (4f) ion, such as rare earth element, exhibit a variety of phenomena due to the competing 4f-3d negative exchange interactions, which arise from the localized and more complex configuration of the 4f orbitals in comparison to the transition metal 3d orbital's [9,106,107]. For instance, spin-reorientation transitions have been reported in a variety of Ortho-ferrites $RFeO_3$ (R = Er, Ho, Nd, Dy, Pr, etc.), and recently in a DP's compound Ho_2CoFeO_6 and the underlying physics was explained by the clash among the magnetic anisotropy and Zeeman energy [108,109]. The spin-glass (SG) phase in a system is a consequence of the spin frustration caused by the presence of competing magnetic interactions that lead to the macroscopically degenerate multiple ground states [110,111]. In the SG state, the connecting spins compete with each other and are unable to acquire long-range magnetic ordering [47,112]. Instead, they freeze in a random way leading to a non-erotic state that is defined by the aging effect, slow spin dynamics, thermo-magnetic irreversibility, and other such features. The exchange bias (EB) phenomenon usually occurs in a system with a magnetic phase separation. The EB effect is induced by the anisotropy that develops as a result of exchange contact at the interface among various magnetic ordered phases [49]. Different types of magnetic interfaces are possible, such as ferromagnetic/ferrimagnetic, ferromagnetic/antiferromagnetic, antiferromagnetic/spin glass, etc. [113]. These days, materials exhibiting significant EB and coercive fields have received a lot of attention due to their application in devices like spin-valves [114], permanent magnets [113], read heads for magnetic recording [115], random access memory [116], and other technologies. The EB effect has also been reported in numerous systems with spontaneous phase segregation. At high temperatures, the compounds in concern usually develop a single phase, but as the temperature decreases, many magnetic phases occur.

The previous report on double perovskite Pr_2CoFeO_6 (PCFO) demonstrates the coexistence of Griffiths phase, re-entrant glassy state, exchange bias, G-type long-range canted antiferromagnetic ordering at $T_N \sim 269$ K, and spin-phonon coupling. Unlike Pr^{3+} (which contains two *4f* electrons), La^{3+} has an absence of *4f* electrons, which will effectively change magnetic interaction. However, substituting larger ions La^{3+} in the place of Pr^{3+} will essentially increase the chemical pressure and may lead to lattice distortion which may affect its magnetic property. Thus, in this report, we have explored the consequence of La^{3+} doping on the Pr^{3+}

site in Pr_2CoFeO_6 double perovskite. Apart from fascinating rich physics, this work will help in predicting many real-life practical applications.

4.2 Experimental details

Polycrystalline sample $Pr_{1.8}La_{0.2}CoFeO_6$ (PLCFO10) was synthesized by the solid-state reaction. High-purity Pr_2O_3, La_2O_3, CoO, and Fe_2O_3 powders were thoroughly mixed in a stoichiometric ratio and were ground for 2 h manually. The mixed powders were placed in Alumina crucibles and annealed at 1060 °C for 25 h (step-up rate 300 °C/h). After cooling it to ambient temperature, a similar annealing procedure was carried out at 1200 °C for 25 h. After that, the powders were ground for 40 minutes and pressed into pellets. The pellets were sintered at 1250 °C for 25 h and were allowed to cool naturally to ambient temperature. The phase purity of the sample was checked using a Miniflex II X-ray diffractometer (Rigaku, Japan) with Cu-Kα radiation (λ = 1.5406 Å). DC and AC magnetization measurements were done using a superconducting quantum interference device (SQUID). The XPS data was collected using a monochromic X-ray source (Al-K line, hν = 1486.70 eV) and a hemispherical electron energy analyzer (E_a = 125 eV) built within an Omicron multi-probe surface research instrument. XPS PEAK-41 peak fit software was utilized to do the fitting of all XPS peaks. The Raman scattering measurements were carried out using a Horiba JY HR-800 spectrometer equipped with an 1800 g mm^{-1} grating and a CCD detector. We utilized a diode laser (λ = 473 nm) as an Excitation source, which was focused onto a 1-µm diameter spot in the backscattering geometry.

4.3 Result and discussion

4.3.1 Structure study

The crystal structure of $A_{2-x}A'_xBB'O_6$ DPs can also be estimated using the tolerance factor (t) [117], using the expression

$$t = \frac{\frac{(2-x)r_A+(x)r_{A'}}{2}+r_O}{\sqrt{2}\left(\frac{r_B+r_{B'}}{2}+r_O\right)} \tag{18}$$

Where r_A, $r_{A'}$, r_B, $r_{B'}$, and r_O indicate the ionic radii of A, A', B, B', and O ions respectively. For the PLCFO10 sample, the determined value of t is 0.84, suggesting an orthorhombic/monoclinic crystal structure for this system.

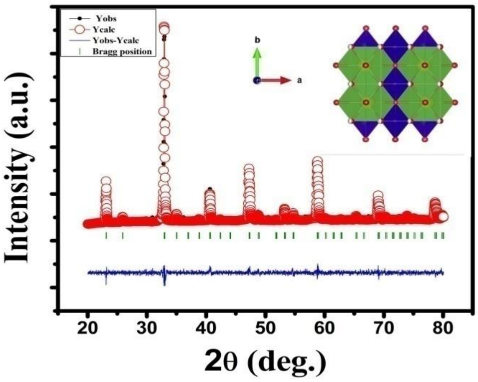

***Fig. 4.1**: The X-ray diffraction pattern with Rietveld refinement and the structure of $Pr_{1.8}La_{0.2}CoFeO_6$ indicating the tilted chains of (Co/Fe) O_6 octahedral with an inset showing the 3D structure.*

Table 1: Structural parameters extracted from the refinement of $Pr_{1.8}La_{0.2}CoFeO_6$.

$Pr_{1.8}La_{0.2}CoFeO_6$	x	y	z	Crystal parameter
La	0.0311(8)	0.25000	0.0137(17)	a = 5.4343(2) (Å)

Pr	0.0311(8)	0.25000	0.0137(17)	b = 7.6854(3) (Å)
Co	0.00000	0.00000	0.50000	c = 5.4394(3) (Å)
Fe	0.00000	0.00000	0.50000	α = 90.0000
O_1	0.503(8)	0.25000	-0.00(6)	β = 90.0000
O_2	0.26(19)	-0.00(6)	0.25(19)	γ = 90.0000
Symmetry = Orthorhombic, Space group = (Pnma)			Reliability factor (χ^2) = 3.2	

In comparison with the end member PCFO (Pnma) and LCFO (R-3c) space groups, the LPCFO (which is 10% doped with Pr at the La site) has an ordered structure consisting of the P21/n space group. Fig 4.1 presents the room temperature XRD pattern of the $Pr_{1.8}La_{0.2}CoFeO_6$ system. The Rietveld refinement of the XRD pattern confirms that the system stabilizes in the orthorhombic crystal structure (space group Pnma) with lattice parameters a = 5.434 Å, b = 7.685 Å, and c = 5.439 Å. The refined crystal structure parameters are summarized in Table 1. It is worth noting that the two extreme components Pr_2CoFeO_6 and La_2CoFeO_6 acquire orthorhombic (Pnma space group) and rhombohedra (space group R-3c) crystal structures respectively [118,119].

4.3.2 X-ray photoemission spectroscopy study

X-ray photoemission spectroscopy (XPS) measurement of our system has been carried out to explore the electronic states of the elements present in our system. The National Institute of Standards and Technology's (NIST) database is utilized to assign the peak positions of the XPS spectrum of our system [120]. Fig 4.2 (a) displays the wide surface scan XPS spectra, which confirm the presence of Pr, La, Co, Fe, and O in the PLCFO. Fig 4.2 (b)-(f) shows the elemental XPS spectra that have been collected individually. Fig 4.2(b) shows the La (3d) XPS spectra which are divided into two peaks, $3d_{5/2}$ and $3d_{3/2}$, because of spin-orbit coupling. These peaks further split into two peaks as a result of core hole occupancy of the La 4f into the $4f^0$ and $4f^1$ states [121]. The doublet peak separation of La (3d) XPS spectra is around 16.6 eV, which indicates La^{3+} valence states in our system [122]. The XPS spectrum of the Pr (3d) core level of the PLCFO demonstrates spin-orbit split peaks ~ 953.6 eV and 933.2 eV, with a doublet separation of 20.4 eV (Fig 4.2(c)). Moreover, two additional exchange splitting features, arising from the coupling of Pr (3d) and Pr (4f) hole states, can be seen near 4.6 eV in the XPS spectrum of the Pr(3d) core level [9,57]. The observed doublet separation implies +3 oxidation states for the Pr ions. Fig 4.2(d) displays the Co (2p) XPS spectra of PLCFO. Owing to the spin-orbit coupling it shows two intense peaks of Co $2p_{1/2}$ and Co $2p_{3/2}$ with a separation of 15.6 eV. The Co (2p) doublet separation in Co_3O_4 (mixed +3 and +2 states) and CoO (divalent Co) is reported to be 15.2 eV and 15.8 eV [123]. It implies that the Co ion in the PLCFO sample has both +2 and +3 valence states. A satellite peak also has been observed in the Co (2p) XPS spectrum near 788.4 eV [124]. This satellite peak is similar to those of the Co_3O_4 compound, confirming the mixed Co^{2+}/Co^{3+} valance state in our system. From the XPS peak fit, we found that the concentration of Co^{2+} is approximately 58%, while the concentration of Co^{3+} is around 42% [125]. The Fe (2p) core-level XPS spectrum of the PLCFO sample is displayed in Fig 4.2(e). Due to spin-orbit coupling, the Fe (2p) spectrum displays doublet $2p_{3/2}$ and $2p_{1/2}$. Peak fitting shows that this doublet is further deconvoluted into two peaks. The peaks at 710.2 and 712.3 eV correspond to $Fe^{3+}(2p_{3/2})$ and $Fe^{4+}(2p_{3/2})$ respectively, while the peaks at 723.5 and 725.0 eV correspond to $Fe^{3+}(2p_{1/2})$ and $Fe^{4+}(2p_{1/2})$ respectively [126]. The peak at 718.5 eV corresponds to the satellite peak of Fe^{3+} ions. The concentrations of the Fe^{3+} and Fe^{4+} ions are estimated to be 55% and 45%, respectively [127]. The spectra of the O1s core level are displayed in Fig 4.2(f). The peak at approximately ~ 529.1 eV is characteristic of O^{2-} ions of lattice oxygen, while the peak at approximately 531 eV ~ 532 eV belongs to electron-deficient oxygen species (viz., O_2^{2-}/O^-) [128,129].

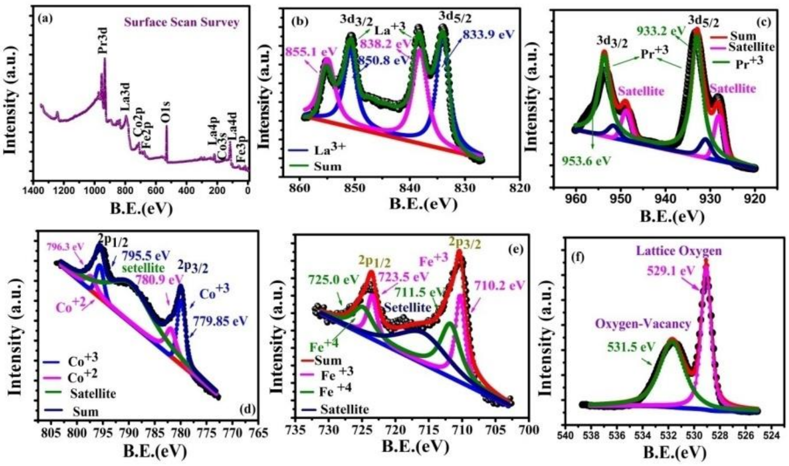

Figure 4.2: *(a)–(f) Wide-range-surface scan & core-level XPS of different constituent elements of* $Pr_{1.8}La_{0.2}CoFeO_6$.

4.3.3 Magnetic study

4.3.3.1 DC magnetization study

The temperature-dependent ZFC and FC magnetization behavior of PLCFO were recorded from 2 to 380 K at a field of 100 Oe (Fig 4.3(a)). This magnetization curve demonstrates a sudden change around 271 K (T_N), which is owing to the long-range magnetic ordering of B-site spins. The exact value of transition temperature was estimated from the point of the inflection of dM/dT *vs.* T curve, as has been shown in the inset of Fig 4.3(a). The FC and ZFC magnetization graphs exhibit large bifurcation below T_N. This bifurcation might be owing to the presence of competition among different magnetic interactions spin frustrations or typical spin-glass states. It is interesting to note that another significant anomaly in the dM/dT *vs.* T curve is observed at 22 K. This suggests the existence of another magnetic phase at low temperatures. To explain this anomaly, we have performed an AC susceptibility measurement which is discussed later in this report. The isothermal M *vs.* H curves at 265 K and 200 K were measured to elucidate the magnetic behavior of the system at T_N ~ 271 K (Fig 4.3(b)). A weak hysteresis behavior can be observed in both curves. This hysteretic nature of the M-H graphs with such a coercive field is a signature of typical canted ferromagnetic or ferrimagnetic substances. Even at a high field of 5 kOe, there is no sign of magnetic saturation; rather, the magnetic moment increases monotonically, demonstrating canted AFM spin ordering [130]. The anti-parallel arrangement of Fe^{3+} spins due to AFM Fe^{3+}/Fe^{4+} interactions essentially provides the AFM nature in the system [131]. To learn more about the nature of spin ordering, we have plotted the Arrott plot (M^2 *vs.* H/M) at the temperatures of 265 K and 200 K, which is displayed in the inset of Fig 4.3(b) [132]. We observed a negative intercept on the M^2 axis by linearly extrapolating the higher field portion of the Arrott plot to H = 0 Oe. This refers to the predominance of the AFM behavior in our sample.

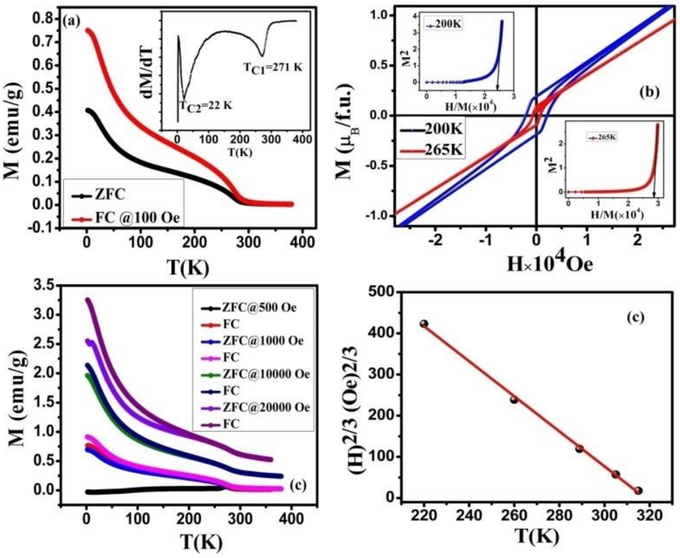

Figure 4.3: *(a) The thermal variation of magnetization graphs at two different applied ZFC and FC conditions. Inset: showing the derivative of the* M_{ZFC}*–T graph to determine the* $T_{C.}$ *(b) M-H graph at a constant temperature near* $T_{C.}$*.inset is showing* M^2 *vs. H/M graph at 200 and*

265 K. (c) The ZFC/FC magnetization of $Pr_{1.8}La_{0.2}CoFeO_6$ at 1 kOe, 5 kOe, and 10 kOe applied field. (d) A graph between the applied field and T_{irr}.

Further, temperature-dependent magnetizations have been measured by applying higher magnetic fields of 500 Oe, 1 kOe, 10 kOe, and 20 kOe for additional analysis. The ZFC and FC curves at fields follow a similar pattern as shown in Fig 4.3(c). The bifurcation between the ZFC and FC curves is observed even at the applied field of 20 kOe. This suggests that the applied field strengths are insufficient to completely align the spins in the direction of the field. It is a signature (but not sufficient) of a spin-glassy nature in the system. Fig 4.3(d) shows T_{irr} (the temperature at which bifurcation starts) shifts towards a lower temperature as the higher field is applied, demonstrating that the frozen phase is relaxed under the influence of an external field. The relationship between T_{irr} and the external magnetic field (H) follows De-Almedia (AT- line) [24,48], where $T_{irr} \alpha H^{2/3}$ [133]. Further, we have presented the χ^{-1} *vs.* T curve of our sample in Fig 4.4(a), which is estimated from 100 Oe FC magnetization measurements. The paramagnetic region of the curve has been fitted using the Curie-Weiss law; which is expressed as

$$\frac{1}{\chi} = \frac{T}{C} - \frac{T_{CW}}{C} \tag{19}$$

Where $C = \frac{N\mu_{eff}^2}{3K_B}$, the T_{CW} (Curie-Weiss temperature) and μ_{eff} (effective magnetic moment) obtained from Curie-Weiss fitting are ~ 249 K and 4.3 μ_B, respectively. A positive sign of T_{CW} signifies the presence of dominating FM interactions within the system. A significant difference between the T_{CW} and T_C values demonstrates the presence of spin frustration in the system [40,134]. The theoretical value of the spin-only moment, μ_{eff} = 4.12 μ_B, is in good agreement with the experimentally determined effective spin-only moment using C-W fit. We have again plotted the temperature variation of the inverse DC susceptibility at various fields, as shown in Fig 4.4(b), to get a better understanding of the system's magnetic properties. We have observed that the 1/χ curve shows a downturn from the Curie-Weiss (C-W) law well above the transition temperature near 360 K (T_G). This divergence from Curie-Weiss law is suppressed at the higher applied magnetic field. This behavior is a feature of the Griffith Phase [34]. In the GP regime at low fields, the 1/χ follows the power law, which is a modified version of the C-W law [120,135].

$$\chi^{-1}(T) \propto (T - T_C^R)^{1-\lambda} \quad (0 < \lambda < 1) \tag{20}$$

Where T_C^R is the critical temperature of random FM and λ is the distinctive non-universal exponent that describes the singularity of the Griffith phase by measuring the deviation from the CW equation. In the complete PM region, the value of T_C^R is selected such that equation (3) gives λ ~ 0. In the paramagnetic region, the Curie temperature, which was acquired using CW fit, is a good choice for T_C^R. The yielded value of λ is ~ 0.91 as has been shown in Fig 4.4(c), suggesting that GP is present in the system.

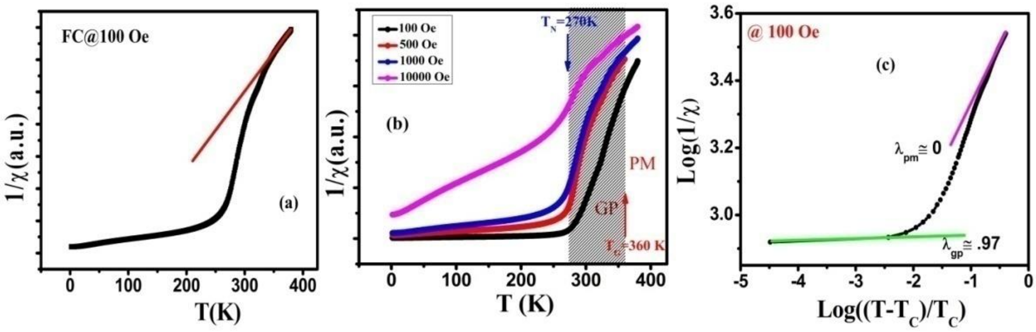

Figure 4. 4: *(a) The inverse susceptibility vs. temperature curves at different fields. (b) Griffith phase graph. (c) Power law fitting.*

4.3.3.2 AC magnetization study

As discussed earlier, the bifurcation in the ZFC and FC magnetization curve suggests the presence of a glassy nature in our system. Thus, we have carried out AC susceptibility measurements, for studying spin dynamics and analyzing glassy behavior [136]. The temperature variation of both the real part [χ' (T)] and imaginary part [χ'' (T)] of the AC susceptibility is presented in Fig 4.5(a) and (b). The graphs χ' (T) demonstrate an anomaly around 34 K, and corresponding dramatic peaks in χ'' (T) are observed at 34 K, which is essential as suggested by the Kramers-Kronig relations [137]. The χ'' (T) peak position demonstrates a shift toward higher temperatures at higher frequencies showing the presence of a glassy dynamic in the system. Thus a low-temperature re-entrant spin glass (RSG) phase is present in our system [138].

To further understand the RSG phase, we have fitted the data with various models. The Mydosh parameter (P) is an empirical parameter for investigating the nature of the glassy phase, which can be determined by analyzing the frequency dependence of the AC peaks. Mydosh parameter is given by [139],

$$P = \frac{\Delta T_f}{T_f \Delta \log_{10}(f)} \tag{21}$$

Where $\Delta T_f = T_{f1}-T_{f2}$ and $\Delta\log_{10}(f) = \log_{10}(f_1) - \log_{10}(f_2)$. The value of P has been used to distinguish the type of glassy state or superparamagnetic state. For the simple SG systems, $P < 0.01$, while for superparamagnetic (SP) systems $P > 0.1$, whereas P values lay 0.01 to 0.1 for the cluster glass (CG). The calculated value of P for our system is ~ 0.03, which shows showing presence of CG in PLCFO.

Furthermore, in a CG or SG phase, the spin movements are slowed down to lower the critical temperature T_f Using the dynamic scaling law (as shown in Fig 4.5(c)), we can investigate the T_f, which is given as [139]

$$\tau = \tau_0(\frac{T_f - T_G}{T_G})^{-zv} \tag{22}$$

Where f shows critical frequency corresponding to the specific spin-flip period ($f_0 = 1/\tau_0$); at the threshold of H_{DC} → 0 Oe and f → 0 Hz, T_G is the analogous spin freezing temperature, and f_0 is the typical spin-flipping time (τ_0) as $f_0 = 1/\tau_0$; zv is called the dynamical critical exponent. In Fig 4.5(c) “spin flip time (τ_0) *vs.* freezing temperature (T_f)” has been plotted and the best fitting with the above dynamical scaling law yielded: (τ_0) ~ 1.2×10^{-4}, T_{SG} ~ 29.8 K, which is near to the observed spin glass freezing temperatures, the exponent zυ is found to be ~ 4.03, which satisfies the spin glass state (4 < zυ < 12) [140,141].

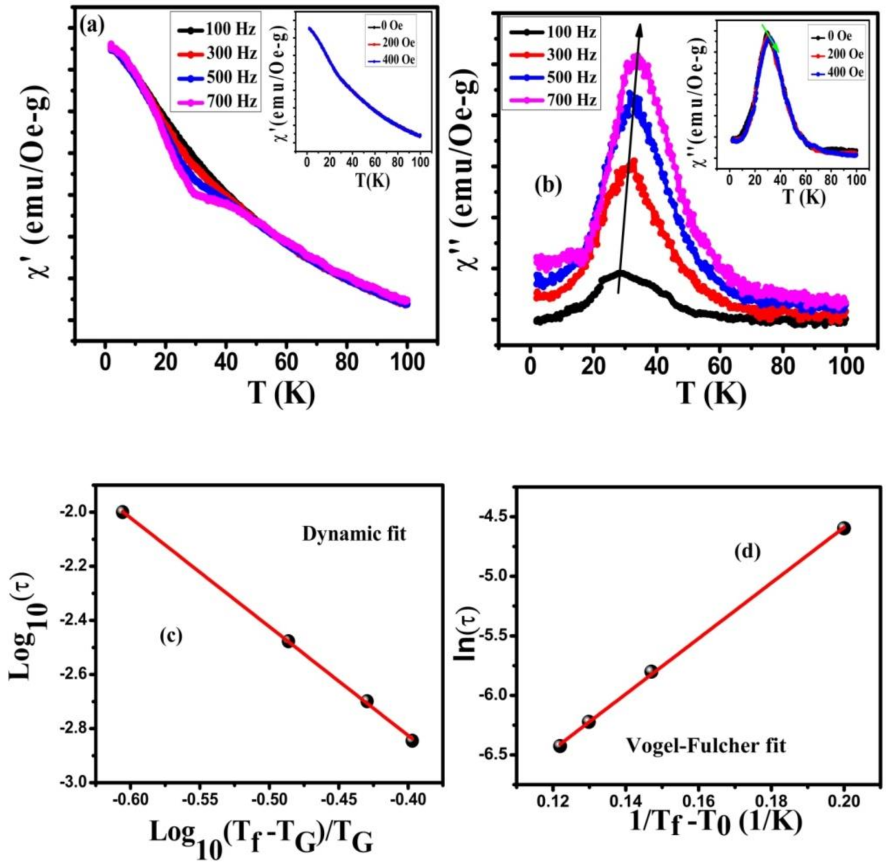

Figure 4.5: *(a) χ' ac curve at different frequencies: inset showing χ' ac at different fields. (b) χ'' ac curve at different frequency .inset: showing χ'' ac at different fields. (c) Dynamic–scaling fitting. (d) Vogel–Fullcher fitting.*

Additionally, the Vogel–Fulcher (V-F) method can be utilized for further investigation of inter-cluster interactions (Fig 4.5(d)) [86]. The model is given by the expression,

$$\tau = \tau_0 \exp\left(-\frac{E_a}{k_B(T_f - T_0)}\right) \tag{23}$$

T_0 is the temperature at which the power of the inter-cluster interaction is reflected by the V-F parameter [142]. Ea is the activation energy, and f_0 is a typical spin-flip time. The best fitting gives $\tau_0 \sim 1.3\times10^{-4}$ (which is of the order of characteristic frequency obtained from earlier dynamic scale fitting), $T_0 \sim 27.2$ K, and $E_a/k_B \sim 23.4$ K.

4.3.3.4 Isothermal Magnetization Study

We measured the isothermal field-dependent (M–H) loop at various temperatures to examine the magnetic properties of the present system in detail, which is shown in Fig 4.6(a). The hysteresis curves at 2 K and 5 K demonstrate nearly identical patterns, with a slightly low magnetization at 2 K (as has been shown in the inset of Fig 4.6(b)). This observation could be attributed to the anti-parallel alignment of paramagnetic Pr^{3+} spins with FM Co/Fe sub-lattice at low temperatures. Another reason for lower magnetization at low temperatures could be owing to the canted spin as canting between the spins rises with decreasing temperature [143]. The hysteresis curves do not acquire saturation up to the maximum applied field of 5 T at both temperatures. The presence of antisite disorder (ASD) in double perovskite is a key reason for unsaturated M-H loops [99], as it introduces various magnetic coupling in the system.

To explain the magnetic characteristics of the La-substituted PCFO at an external field, isothermal magnetization M *vs.* H measurements have been carried out up to a field ± 5 T at 2, 5, 25,100, 200,265, and 320 K, respectively in ZFC mode. For the objective of studying more analysis into the characteristics of the glassy behavior, we have collected M *vs.* H graphs at various temperatures, as displayed in Fig 4.6(a). It has been observed in Fig 4.6(c) that the magnetic hysteresis loop increased significantly after the temperature decreased to 265 K suggesting there has been an effective increase in FM interaction strengths [144]. However, as the temperature decreased further to 125 K, it was interesting to observe that the squareness of the closed path (which signifies the FM phase) finished with an increase in coercivity but a decrease in remanence. This could be a possible sign that the system is about to enter a glassy phase. However, no saturation of magnetic moment can be observed at any of the temperatures, which suggests that the AFM nature of the material is predominating [145]. Nevertheless, the M *vs.* H loop demonstrates an enhanced magnetization value at 5 K, although it has disappeared its squareness. This could be also explained by the existence of magnetic rare earth Pr^{3+} ions since these ions set off complex, short-range Pr^{3+}-Fe^{3+} and Pr^{3+}-Fe^{3+} interactions, which are effective only at low temperatures [146]. Co has varying valence and spin states. Co^{3+} ions with $3d^6$ electron configuration have three spin states: low-spin S = 0, intermediate-spin S = 1, and high-spin S = 2. The variety of Co^{3+} spin states has prompted interest in cobalt, particularly for spin-crossover phenomena such as applied magnetic fields or variations in temperature [147].

In the field-dependent magnetization study, of PLCFO, another significantly unique and interesting meta-magnetic behavior is noticed. The ZFC magnetization curves obtained under different fields are shown in Fig 4.6(d). Under a low field of 100 Oe, the M (T) curve increases gradually as temperature decreases. To our surprise, the M (T) curve demonstrates an abrupt decrease and produces a peak below the ordering temperature at an increased applied magnetic field of 500 Oe. However, as applied fields rise (1 kOe, for example), the peak flattens and broadens. With further increasing fields, the peak begins to decrease and finally disappears for the field >1 T. It is possible that the enormous anisotropy that is present in the system, can help to clarify the occurring field-induced transition. It would appear that the field of 100 Oe was insufficient for the total anti-parallel arrangement of the Fe^{3+} spins. Therefore, the existence of some unsaturated spins in the system is evidenced by the steady increase in magnetization with a moderate field (100 Oe). At an intermediate field of 600 Oe, however, the Fe^{3+} spins are completely aligned antiparallel to one another, causing the magnetization to decrease significantly and approach a peak [143]. At a higher field, it will attempt to align the Fe^{3+} spins in the direction of the field, which will diminish the peak. The application of strong fields that suppress the peak intensity is a usual nature of AFM systems.

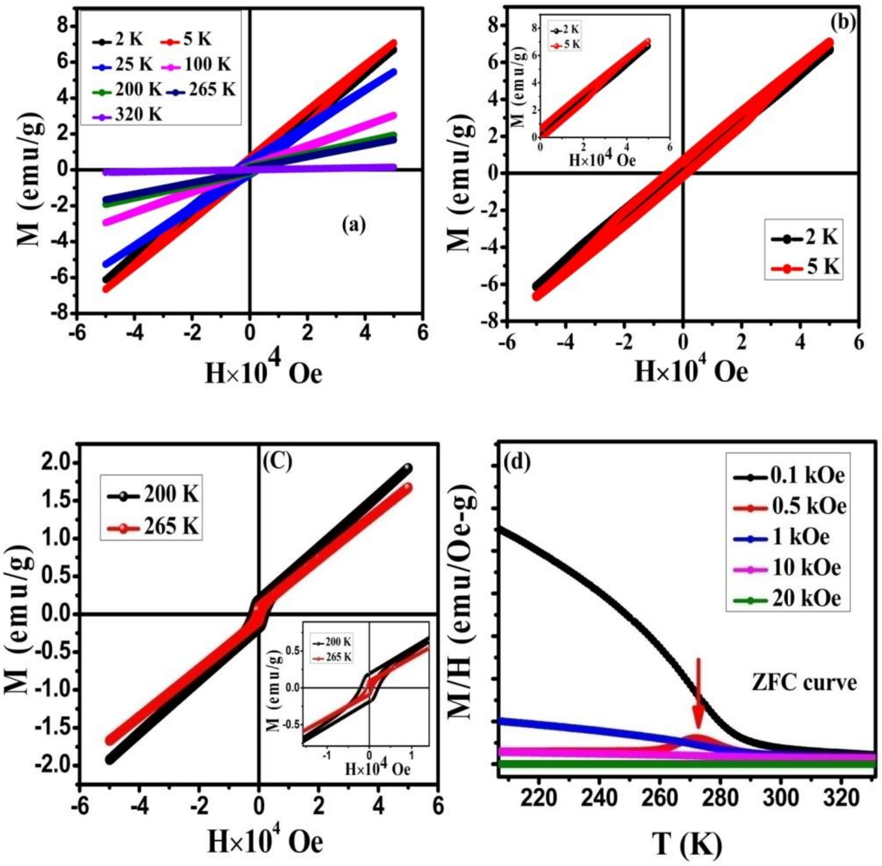

***Figure 4.6**: (a) The isothermal magnetizations vs. magnetic field of $Pr_{1.8}La_{0.2}CoFeO_6$at different temperatures. (b) M-H curve at 2 K and 5 K. (c) M-H curve at 200 K and 265 K. (d) χ_{dc} vs. temperature graph at 100 Oe.*

4.3.3.5 Exchange Bias Effect

Exchange bias (EB) usually occurs when numerous inhomogeneous magnetic phases (FM/SG, FM/Ferrimagnet, AFM, soft/hard states of FM systems, etc.) coexist in a system. The system PLCFO exhibits many magnetic phases like FM/AFM, SG, and CG phases, which guides us to study the EB effect on this system [148]. The M (H) graph shifts towards the positive magnetization axis and the negative magnetic axis below 100 K, mainly as an impact of the EB effect. PLCFO has been demonstrated to have both the conventional exchange bias (CEB) and spontaneous exchange bias (SEB) effects at low temperatures. The mathematical expressions of the EB field (H_{EB}) and coercive field (H_C) are, respectively, $H_{EB} = (H_R + H_L)/2$ and $H_C = (|H_R| + |H_L|)/2$, where H_R and H_L are the right and left coercive fields. The mathematical expressions of the remanent magnetization (M_R) and EB Magnetization (M_{EB}) are, respectively, $M_R = (|M_{R1}| + |M_{R2}|)/2$ and $M_{EB} = (M_{R1} + M_{R2})/2$ where M_{R1} and M_{R2} are the two cuts of the Magnetization axis [131,149,150]. The M *vs.* H curves could shift vertically and horizontally due to the uncompensated minor loop effect [149]. Therefore, we have measured the M *vs.* H graph at 5 K by cooling the system in both ± 50 kOe magnetic fields to rule out such an effect for PLCFO. Fig 4.7 demonstrates that for cooling fields of +50 kOe, the M-H graph moved towards the positive side of the field axis while for cooling fields of -50 kOe, it was shifted towards the negative side. As a result, the prospect of an uncompensated minor loop effect was eliminated as a result of this observation [150].

As the magnetization value does not saturate up to such a higher field, the figure demonstrating the M *vs.* H graph at 5 K with ± 50 kOe field provides evidence of the dominant AFM constituent in the system as shown in Fig 4.7. This M *vs.* H graph is also completely displaced in both the positive magnetization axis and the negative field axis. As a consequence of its asymmetry, the M *vs.* H hysteresis graph of PLCFO at 5 K displays the SEB effect. H_{SEB} is calculated as ~ 1.8 kOe and M_{SEB} 0.260 emu/g. At the same temperature, the CEB effect has also been studied in FC conditions. When the sample was frozen in a ± 5 Tesla applied field and the M *vs.* H graph was estimated at 5 K, the PLCFO sample showed a significant CEB effect. After cooling the sample to 5 K while maintaining a +5 Tesla applied field in the field-cooled condition, a significant shift in M *vs.* H was seen towards the positive magnetization axis and the negative field axis, which was related to the CEB effect. An equal amount of shift was seen in the other direction, i.e., the + ve field axis and the - ve magnetization axis, as displayed in figure 4.7, when FC was performed for a -5 Tesla applied field and the M *vs.* H graph was taken at 5 K. The shifting in M -H graphs for the maximal +ve and -ve fields are very similar, demonstrating that the cause of the graph shifting is not a minor loop effect [151]. Under FC conditions, the shift in M-H graphs known as the CEB field (H_{CEB}) has a huge value (H_{CEB} ~ 2.4 kOe).

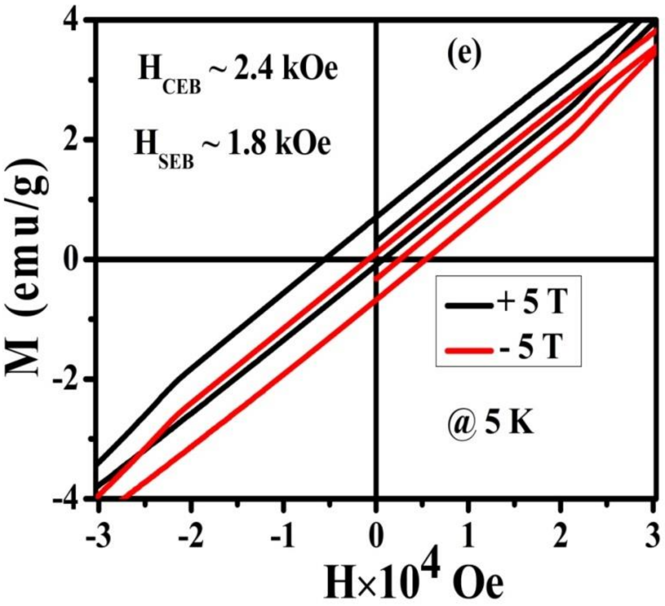

Figure 4.7*: Exchange bias effect at 5 K with applied field +5 T and -5 T.*

4.3.4 Raman spectroscopy

Raman spectroscopy is probed to study the changes in structural properties such as symmetry, disorder, cationic ordering, and localization. The Raman spectra of cubic systems(space group Pm3m), where all the atoms are arranged in a Centro-symmetric way, have no active phonon modes [152–154]. For the orthorhombic structure (Pnma), the group theory studies propose 60 Γ-point phonon modes. These modes can be split into 8 silent modes, 24 Raman active modes (7A1g+5B1g+7B2g+5B3g), 25 infrared active modes, and 3 acoustic modes [155,156]. Fig 4.8(a) demonstrates the room temperature Raman spectra of the PLCFO system. It is observed that 6 out of the 24 Raman active modes are visible; with the 650 cm^{-1} peak having the highest intensity. In all the observed Raman modes only two bands (ω_1 ~ 539 cm^{-1} and ω_2 ~ 650 cm^{-1}) are visible for the whole measured temperature range Fig 4.8(b). The phonon modes that emerge from the movement of heavy rare earth ions show up below 200 cm^{-1} while the modes that are visible beyond 300 cm^{-1} are only caused by the movement of oxygen cations. The Co/Fe (B-site) ions are Centro-symmetric, as mentioned before; hence they do not contribute to these modes. Consequently, the mobility of oxygen in the (Co/Fe) O_6 octahedral corresponds to both of the observed peaks. The bands observed at approximately ~ 539 cm^{-1} and ~ 650 cm^{-1} correspond to the anti-stretching and stretching vibrations of the (Co/Fe) O_6 octahedral, respectively [152,153,156,157]. It is an acceptable fact that the number of Raman active peaks for the disordered DPs should not change from that of the single perovskite, either RBO_3 or $RB'O_3$.

Fig 4.8(b) demonstrates the experimental Raman spectrum for PLCFO that was collected at different temperatures between 80 K and 300 K. The absence of any structural transition in the temperature range of 80-300 K is demonstrated by the absence of any extra mode and the absence of any significant shape change in the system. Furthermore, spin-phonon coupling across T_C is shown by the unusual behavior in the Ag mode position. Y_2CoMnO_6, Y_2NiMnO_6, La_2CoMnO_6, Pr_2CoMnO_6, Nd_2CoMnO_6, and other ordered DP systems (P21/n) genuinely show some low-intensity Raman modes in addition to the two main intense anti-stretching and stretching modes [125,158]. They are explained by the system's B-site cationic ordering.

Conversely, systems with disordered orthorhombic (Pnma) structures exhibit less number of Raman modes than those with ordered monoclinic (P21/n) structures.

The impact of temperature on the Ag mode is also displayed clearly in Fig 4.8(c). According to Balkanshi, in the absence of any structural transition and any coupling between spin and phonon, the phonon frequency would follow the anharmonic nature. The phonon excitation wave number in this model is defined in the following manner [159],

$$\omega_{\mathrm{anh}} = \omega_0 - \mathrm{C}\left(1 + \frac{2}{e^{\frac{h\omega_0}{K_B T}} - 1}\right) \tag{24}$$

Where k_B is Boltzmann's constant, h is Planck's constant. T is the temperature, and C and ω_0 are versatile parameters. This function suggests that for a given mode, the phonon frequency should gradually harden with a lowering temperature and form a plateau at sufficiently low temperatures [57]. Fig 4.8 (c) illustrates the phonon mode hardening for the stretching mode down to a temperature of T_N ~ 270 K. Thus, it is evident that the temperature dependence of the phonon excitation of PLCFO is mostly influenced by anharmonicity. Remarkably, Fig 4.8(c) shows that, below the magnetic transition temperature T_N, the stretching mode deviates from the anharmonic behavior. However, for the stretching mode, the theoretical curve achieves the plateau region after going down to a sufficiently low temperature (below 150 K), after which it continues to harden, however, the experimental curve has an enormous change in slope and demonstrates anomalous softening below T_N. Therefore, the observation of anomalous phonon mode softening (near T_N) (which involves magnetic Fe ion vibrations) suggests effective modulation of the lattice vibrations due to magnetic ordering, which corresponds to the spin-phonon coupling.

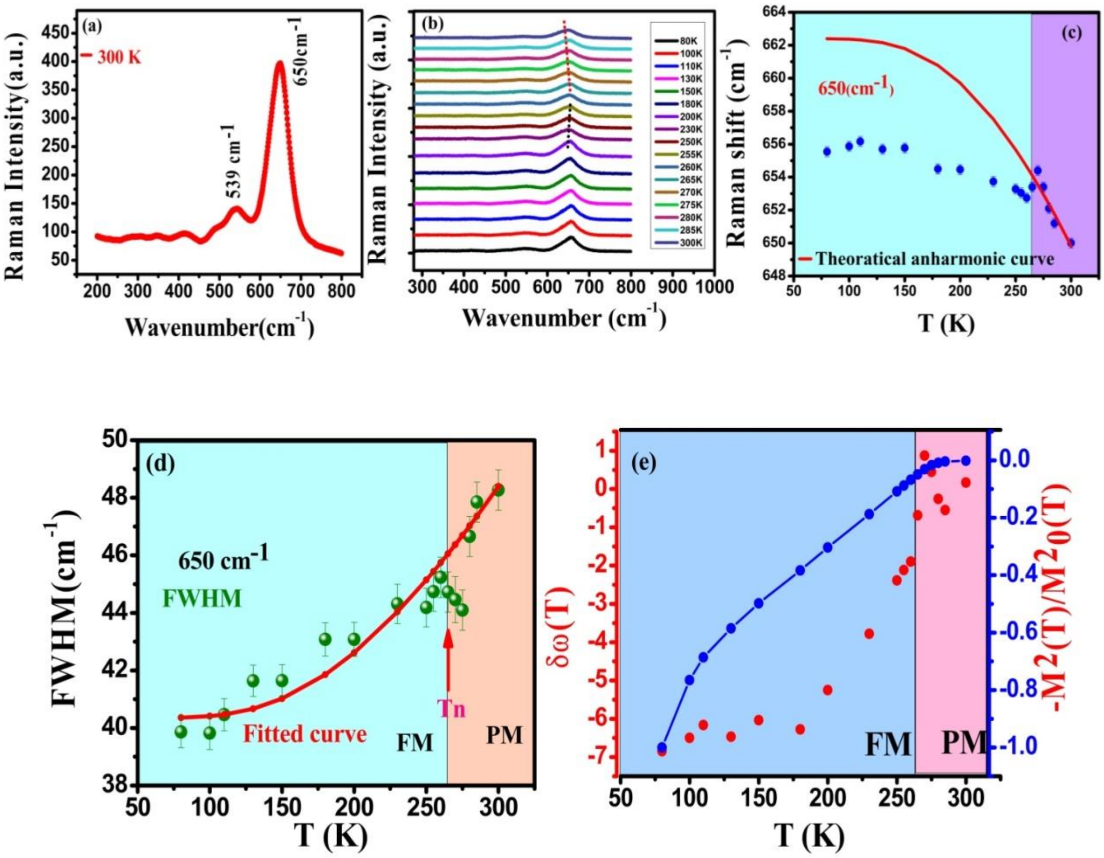

Figure 4.8*: (a) Raman spectrum at room temperature. (b) Depicts Raman spectra at different temperatures. (c) Shows the anharmonic fitting to the temperature-dependent Raman shift of stretching mode. (d) Presents temperature variation of the FWHM of the stretching mode with an anharmonic fit. (e) Thermal variation of* $\delta\omega$ *(T) and* $(\mathrm{M(T)/M\,(T_0)})^2$ *of Anti-stretching mode.*

The anomalous temperature variation of the phonon frequency might also be caused by the magneto-striction effect. Therefore, it is essential to understand the exact cause of the phonon anomaly the magneto-striction, or the spin-phonon coupling. In reality, the slight variations in the lattice/volume parameters caused by the magneto-striction effect do not affect the full width at half maximum (FWHM) of the applicable phonon exactions [137,160]. Instead, since FWHM is correlated to the phonon delay process, it can be affected by the anomalous spin-phonon coupling that occurs across the magnetic transition. Fig 4.8(d) displays the corresponding graph of FWHM *vs*. temperature. Remarkably, for the given mode, the FWHM displayed an unusual broadening below T_N ~ 270 K, indicating a unique deviation from the expected anharmonic behavior. Thus, the observed anomalous FWHM broadening can be explained by a decrease in phonon lifetime beyond T_N, which corresponds to the activation of some more phonon decay modes due to phonon entanglement with underlying long-range magnetically ordered spins [161]. Two basic factors, particularly electron-phonon coupling and spin-phonon coupling, are generally responsible for changes in phonon lifetime. Nevertheless, the present XPS analysis, together with another experimental research on this system, demonstrated that it is an insulator, easily ruling out any possibility of electron-phonon coupling. It is therefore clear that the spin-phonon coupling in PLCFO is the cause of the observed FWHM anomaly [162].

Additionally, the mean field approximation suggests a renormalization of the phonon frequency occurs when long-range magnetic ordering establishes a place in a structure [159,163,164]. The phonon renormalization is found to be proportional to the spin-spin correlation function ($<S_j.S_k>$), where S_J and S_K denote the nearest neighbor spins at the j_{th} and k_{th} sites, respectively. The phonon frequency change caused by this renormalization demonstrates the same patterns as the normalized magnetization, which leads to the following expression:

$$\delta\omega\ (T) = \omega(T) - \omega_{anh}(T) = \left(\frac{M^2(T)}{M_0^2}\right) \tag{25}$$

Where M_0 is the saturation magnetization and M (T) is the temperature-dependent average magnetization. We have thus displayed in Fig 4.8(e) the temperature variations of $(M\ (T)/M\ (T_0))^2$ and δω (T) for the given phonon mode to further examine spin-phonon coupling. The data demonstrate that $(M\ (T)/M_0)^2$ and δω (T) exhibit a comparable trend, with a downturn almost occurring at the same temperature (T_N ~ 270 K). This could be caused by the system having different magnetic ordering, such as FM, AFM, and spin glass phases, each of which contributes to various exchange interactions and, eventually, a different phonon renormalization [124]. Similar diverges from the mean-field concepts have been observed in a few additional systems, such as Pr_2CoFeO_6, La_2CoMnO_6, $Sr_{0.6}Ba_{0.4}MnO_3$, Y_2CoMnO_6, and so on, where the coexistence of complex AFM/FM and/or spin glass state enhances the complexity of the spin-phonon coupling process [164,165].

4.5 CONCLUSION

In summary, the structural study shows that PLCFO acquires orthorhombic crystal structure with the Pnma space group. X-ray photoemission spectroscopy (XPS) demonstrated the presence of both B-site ions in mixed valence states (Co^{2+}/Co^{3+}) and (Fe^{3+}/Fe^{4+}). Magnetometer observations of the system indicate the presence of numerous intriguing magnetic behaviors, including long-range anti-ferromagnetic (canted) ordering (T_N = 271 K), huge exchange bias, and re-entrant cluster glass (RCG) phase (T_G = 33 K). At 5 K, field-dependent magnetization exhibits a significant spontaneous exchange bias (H_{SEB}) of approximately 1.8 kOe and a massive conventional exchange bias (H_{CEB}) of around 2.4 kOe. Temperature-dependent Raman analysis revealed that the observed phonon behaves abnormally around the magnetic transition temperature (T_N = 271 K). An interesting abnormal softening was seen below T_N, indicating the presence of strong spin-phonon coupling, but the magnetostriction effect had no significant involvement in the observed phonon anomalies.